Supplementary Material for Ferroelectric phase transition and the lattice thermal conductivity of $Pb_{1-x}Ge_xTe$ alloys

Ronan M. Murphy[1,2], Éamonn D. Murray[3], Stephen Fahy[1,2], and Ivana Savić[2]

[1] *Department of Physics, University College Cork, College Road, Cork, Ireland*

[2] *Tyndall National Institute, Dyke Parade, Cork, Ireland and*

[3] *Department of Physics and Department of Materials, Imperial College London, London SW7 2AZ, UK*

(Dated: March 5, 2017)

I. CHOICE OF SUPERCELL SIZE

We carried out lattice thermal conductivity calculations using $4 \times 4 \times 4$ (128 atom) supercells because they reproduced the expected physical behavior of the second-order phase transition in $Pb_{1-x}Ge_xTe$ alloys. We found that the continuity of harmonic interatomic force constants (IFCs) at the phase transition leads to physically sensible phonon dispersions in the rhombohedral phase. In $2 \times 2 \times 2$ cubic (64 atom) supercells discontinuities were found in the long-range IFCs (4th and 8th nearest neighbor) for the rocksalt and rhombohedral structures very near the phase transition, $x = 0.49$ and $x = 0.51$ respectively. This resulted in imaginary frequencies for the lowest transverse acoustic mode near Γ in rhombohedral structures close to the phase transition. These instabilities were found to persist for larger supercells such as $3 \times 3 \times 3$ cubic (216 atoms), $5 \times 5 \times 5$ (256 atoms) and $4 \times 4 \times 4$ cubic (512 atoms). On the other hand, using density functional perturbation theory, we found that the frequencies of transverse acoustic modes for rhombohedral structures near the phase transition exhibit oscillations about the physically correct linear dependence on the wave vector near Γ along the $\Gamma-$ X direction. While these oscillations decreased in magnitude with denser wave vector grids, they nevertheless remained for rhombohedral Brillouin zone grid sizes up to $12 \times 12 \times 12$. While this suggests that larger supercells would be required to overcome these issues, such calculations would presently be computationally very demanding. Thus, we chose $4 \times 4 \times 4$ (128 atom) supercells as they possess continuity in the IFCs at the second-order phase transition (see Fig. 7 of the paper), and exhibit the physically correct linear dependence of the acoustic mode frequencies on the wave vectors near Γ. However, further investigation is necessary to better understand the effect of these long range interactions in $Pb_{1-x}Ge_xTe$ alloys.

II. VERIFICATION OF OUR COMPUTATIONAL APPROACH

To verify the validity of our approach, we compare our calculated phonon band structure, thermal expansion coefficients and lattice thermal conductivity κ on $4 \times 4 \times 4$ (128 atom) supercells for PbTe and GeTe with experimental data. We also included the validation of our computed third-order IFCs through Grüneisen parameter calculations.

The phonon dispersion of PbTe for 128 atom supercells is in good agreement with the

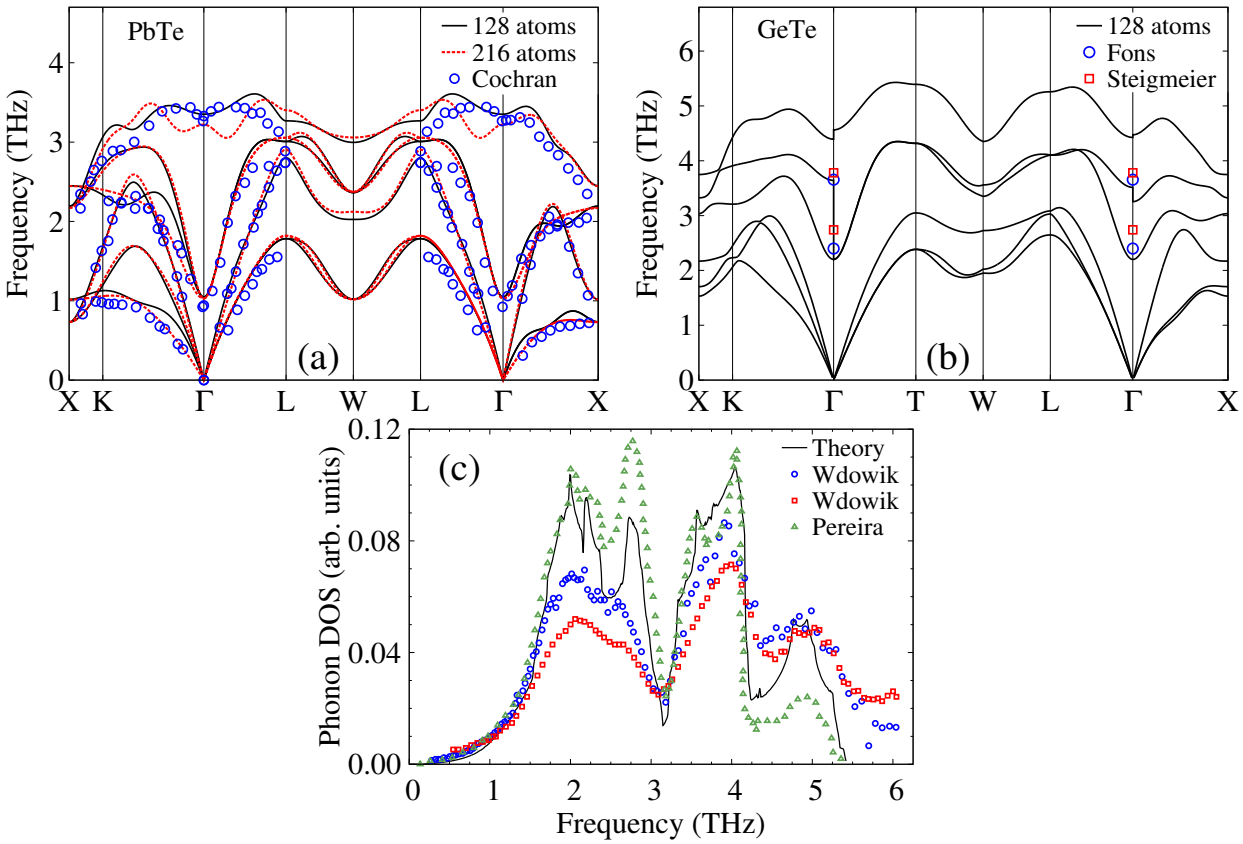

FIG. 1. (a) Phonon dispersions of PbTe: calculated using 128 atoms supercell at 0 K (solid black line), calculated using 216 atoms supercell at 0 K (dotted red line), and measured by Cochran *et al.* [1] at 300 K (blue circles). (b) Phonon dispersions of GeTe: calculated using 128 atoms supercell at 0 K (solid black line), and the frequencies of zone centre Raman active modes measured by Fons *et al.* [2] at 300 K (blue circles) and Steigmeier *et al.* [3] at 300 K (red squares). (c) Phonon density of states for GeTe: calculated using 128 atoms supercell at 0 K (solid black line), measured by Wdowik *et al.* [4] and Pereira *et al.* [5]. The integral of the density of states over frequency is normalized to unity.

inelastic neutron scattering measurements of Cochran *et al.* [1] (see Fig. 1 (a)), except for transverse modes along Γ-X and Γ-K directions. Our computed dispersion for 216 atom cubic supercells does not exhibit such deviations from the experiment. However, as discussed in detail in Section I, we can describe correctly the second order phase transition behavior across the whole range of alloy compositions only using 128 atom supercells. Our calculated

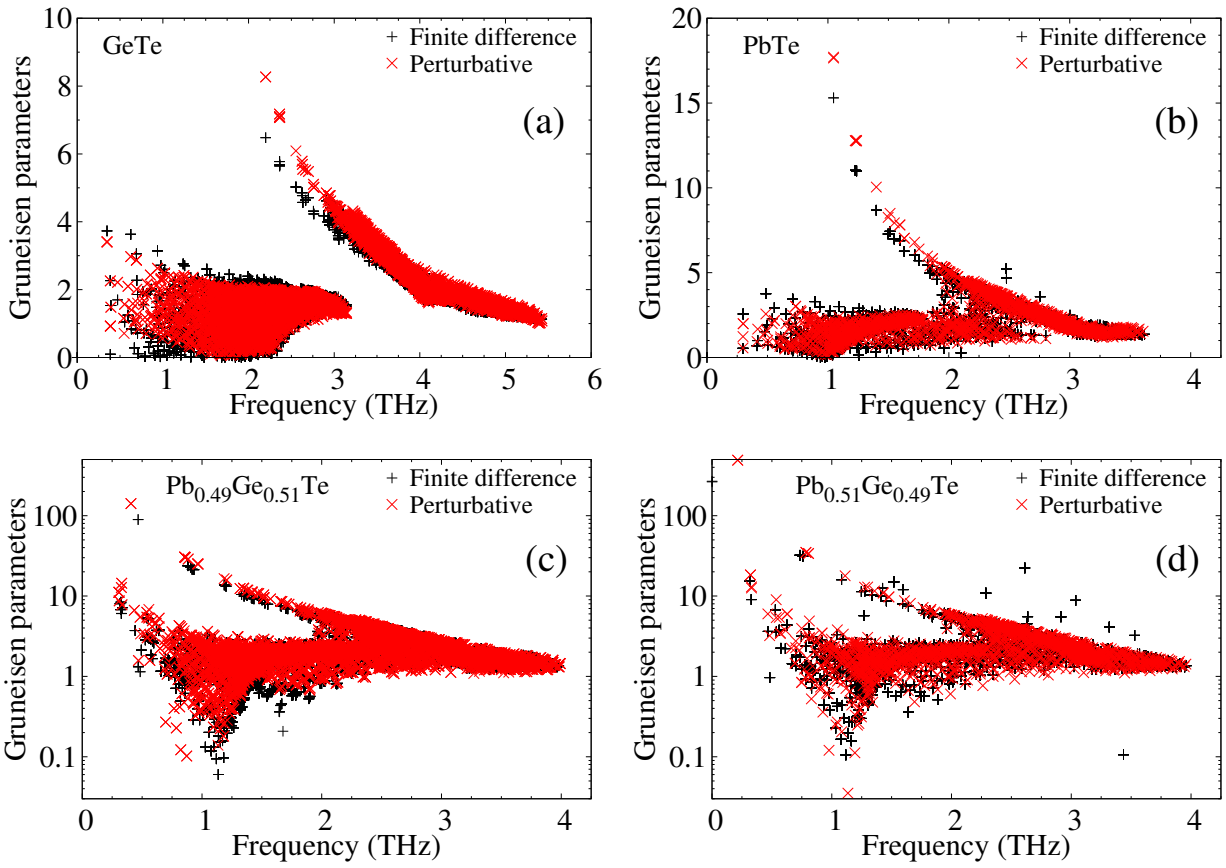

FIG. 2. Mode Grüneisen parameters as a function of frequency obtained using finite difference (black pluses) and perturbative approaches (red crosses) for (a) GeTe, (b) PbTe, (c) $Pb_{0.49}Ge_{0.51}Te$, and (d) $Pb_{0.51}Ge_{0.49}Te$.

phonon dispersion of GeTe for 128 atom supercells is shown in Fig. 1 (b). To the best of our knowledge, there are no reports of the measured phonon dispersions of GeTe in the literature. Our computed frequencies of zone center Raman active modes compare well with the measurements of Refs. [2, 3] at 300 K. We also calculated the phonon density of states of GeTe (Fig. 1 (c)), which is in good agreement with the experimental results of Refs. [4, 5]. Our phonon dispersion of GeTe also agrees well with a previous density functional perturbation theory calculation [6].

We verified the accuracy of our computed third-order anharmonic interatomic force constants (IFCs) by calculating the mode Grüneisen parameters of $Pb_{1-x}Ge_xTe$ alloys using two different approaches. Mode Grüneisen parameters are defined as

$$\gamma_{\mathbf{q},s} = -d(\log \omega_{\mathbf{q},s})/d(\log V), \tag{1}$$

where (**q**,s) denotes the wave vector **q** and branch index s of a phonon mode with frequency $\omega_{\mathbf{q},s}$, and V is the primitive cell volume. To calculate $\gamma_{\mathbf{q},s}$, we used a finite difference approach that requires computing phonon frequencies at different crystal volumes using Eq. (1). We also used a first-order perturbative approach to express Grüneisen parameters in terms of third-order anharmonic IFCs [7]:

$$\gamma_{\mathbf{q},s} = -\frac{1}{6\omega^2_{\mathbf{q},s}} \sum_{\mathbf{l}',\mathbf{l}''} \sum_{\mathbf{b},\mathbf{b}',\mathbf{b}''} \sum_{\alpha,\beta,\gamma} \Psi_{\alpha\beta\gamma}(\mathbf{0b}, \mathbf{l}'\mathbf{b}', \mathbf{l}''\mathbf{b}'') \frac{e^*_\alpha(\mathbf{b}|\mathbf{q}s) e_\beta(\mathbf{b}'|\mathbf{q}s)}{\sqrt{m_\mathbf{b} m_{\mathbf{b}'}}} \exp(i\mathbf{q}\mathbf{l}') r_\gamma(\mathbf{l}''\mathbf{b}''). \quad (2)$$

l is the position vector of a unit cell, **b** represents an atom in the unit cell **l** with mass $m_\mathbf{b}$, and α, β and γ are Cartesian coordinates. $\Psi_{\alpha\beta\gamma}(\mathbf{0b}, \mathbf{l}'\mathbf{b}', \mathbf{l}''\mathbf{b}'')$ are the third order IFCs, and $e_\alpha(\mathbf{b}|\mathbf{q}s)$ represents the component of the eigenmode $(\mathbf{q}, s)$ that corresponds to the atom **b** along the α direction. $r_\gamma(\mathbf{lb})$ is the component in the γ direction of the position vector of the atom **lb**. Eq. (2) is derived under the assumptions that the crystal is cubic, and the atomic positions within the crystal remain fixed upon volume changes. This condition is not fully satisfied for rhombohedral lattices. Consequently, to compare the mode Grüneisen parameters obtained with Eq. (2) with those of the finite difference approach for nearly cubic $Pb_{1-x}Ge_xTe$ alloys, we varied only their lattice constants in the finite difference calculations. Fig. 2 shows the Grüneisen parameters in the whole Brillouin zone obtained using the two described approaches for GeTe, PbTe, and the alloy compositions near the phase transition, $Pb_{0.49}Ge_{0.51}Te$ and $Pb_{0.51}Ge_{0.49}Te$. The results obtained from the two approaches agree very well with each other for all these materials, which confirms the accuracy of our computed third-order IFCs.

We also computed the linear thermal expansion coefficient of PbTe as [8]

$$\alpha = \frac{1}{3NVB} \sum_{\mathbf{q},s} c_{\mathbf{q},s} \gamma_{\mathbf{q},s}, \quad (3)$$

where $c_{\mathbf{q},s}$ is the heat capacity, B is the bulk modulus and N is the total number of sampled **q**-points. Our calculated bulk modulus of PbTe is 47.94 GPa. Fig. 3 shows the linear thermal expansion coefficient of PbTe versus temperature obtained with the Grünesien parameters computed using the perturbative approach, and illustrates good agreement with the measurements on single crystalline PbTe samples [9, 10].

We also derived the generalized expressions for the thermal expansion coefficients of the rhombohedral lattice in a similar manner as done in Ref. [11], and calculated these coefficients for GeTe. The relative positions of Ge and Te atoms within the rhombohedral

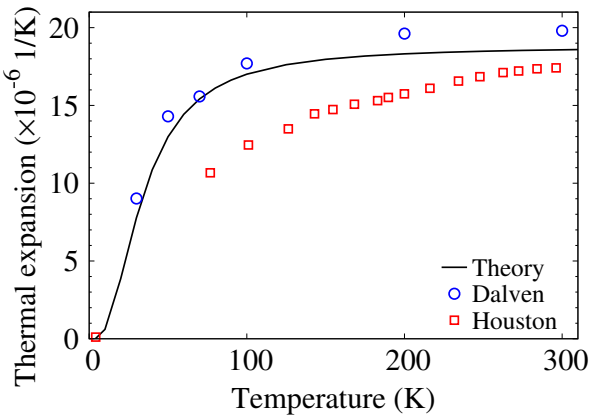

FIG. 3. Linear thermal expansion coefficient of PbTe as a function of temperature: calculated using a 128 atom supercell (solid black line), measured by Dalven [9] (blue circles), and measured by Houston *et al.* [10] (red squares).

primitive cell are $(0,0,0)$ and $(0.5+r, 0.5+r, 0.5+r)$ with $r = 0.0237$ in our calculations, and the angle between the lattice vectors is $\phi = 60° - \theta$ with $\theta = 1.2093°$. The change of the zero temperature total energy with respect to the small deviations of the lattice constant a, the angle ϕ and the Te displacement along the [111] direction r is given as

$$\Delta E = \frac{1}{2}C_{aa}(\Delta a)^2 + \frac{1}{2}C_{\phi\phi}(\Delta\phi)^2 + \frac{1}{2}C_{rr}(\Delta r)^2 + C_{a\phi}(\Delta a)(\Delta\phi) + C_{ar}(\Delta a)(\Delta r) + C_{\phi r}(\Delta\phi)(\Delta r). \tag{4}$$

We calculate the symmetric matrix $[C]$ using density functional theory, and find its inverse matrix $[S] = [C]^{-1}$. The thermal expansion coefficients for a, ϕ and r can be expressed as:

$$\alpha_a = \frac{1}{Na}\sum_{\mathbf{q},s} c_{\mathbf{q},s}\left(\frac{S_{aa}}{a}\gamma^a_{\mathbf{q},s} + \frac{S_{a\phi}}{\phi}\gamma^\phi_{\mathbf{q},s} + \frac{S_{ar}}{r}\gamma^r_{\mathbf{q},s}\right), \tag{5}$$

$$\alpha_\phi = \frac{1}{N\phi}\sum_{\mathbf{q},s} c_{\mathbf{q},s}\left(\frac{S_{a\phi}}{a}\gamma^a_{\mathbf{q},s} + \frac{S_{\phi\phi}}{\phi}\gamma^\phi_{\mathbf{q},s} + \frac{S_{\phi r}}{r}\gamma^r_{\mathbf{q},s}\right), \tag{6}$$

$$\alpha_r = \frac{1}{Nr}\sum_{\mathbf{q},s} c_{\mathbf{q},s}\left(\frac{S_{ar}}{a}\gamma^a_{\mathbf{q},s} + \frac{S_{\phi r}}{\phi}\gamma^\phi_{\mathbf{q},s} + \frac{S_{rr}}{r}\gamma^r_{\mathbf{q},s}\right), \tag{7}$$

respectively, where we generalized Grüneisen parameters as $\gamma^a_{\mathbf{q},s} = -\partial(\log\omega_{\mathbf{q},s})/\partial(\log a)$, $\gamma^\phi_{\mathbf{q},s} = -\partial(\log\omega_{\mathbf{q},s})/\partial(\log\phi)$ and $\gamma^r_{\mathbf{q},s} = -\partial(\log\omega_{\mathbf{q},s})/\partial(\log r)$. Finally, for comparison with experiment, we transformed the obtained expressions into the coordinate system of the non-primitive pseudo-cubic lattice vectors where the lattice constant is given as $A = a(3 - 2\cos\phi)^{1/2}$, the angle between lattice vectors is $\cos\Phi = (2\cos\phi - 1)/(3 - 2\cos\phi)$, and the

TABLE I. Thermal expansion coefficients α of GeTe at 300 K for lattice constant A, the angle between the lattice vectors Φ, and the Te atom position along the [111] direction R in the non-primitive pseudo-cubic lattice. The thermal expansion coefficients from Refs. [12–16] were extracted by linearly fitting the measured lattice parameters between ~ 300 K and $\sim 400 - 550$ K.

	Our results	Ref. [12]	Refs. [13, 14]	Ref. [15]	Ref. [16]
sample	single crystal	single crystal	powder	powder	powder
α_A (10^{-6} 1/K)	12.3	13.4	12.9	18.7	17.4
α_Φ (10^{-6} 1/K)	7.7	23.3	27.6	23.0	32.3
α_R (10^{-6} 1/K)	15.5	16.9	49.5	–	–

Te position along the [111] direction is $R = 0.25 - r/2$. The comparison of our computed thermal expansion coefficients for A, Φ and R of GeTe at 300 K with the experimental values [12–16] is given in Table I. We extracted the experimental coefficients by linearly fitting the reported lattice parameters between ~ 300 K and $\sim 400 - 550$ K. Our computed thermal expansion coefficients are in reasonable agreement with experiments. We ascribe the discrepancies to our zero temperature representation of structural parameters and IFCs and the quasiharmonic approximation, as well as the uncertainties in fitting the sparse experimental data.

Our calculated κ of PbTe is $\sim$20% larger than the κ of undoped ($\sim 10^{17}$cm^{-3}) single- and poly-crystalline PbTe measured with the absolute steady-state technique [17] for 100-300 K, see Fig. 4 (a). For higher temperatures of 300-700 K, we see very good agreement between our calculated κ compared to undoped poly-crystalline PbTe measured using the plane temperature waves technique [18]. However, the agreement for higher temperatures is somewhat accidental, as higher order anharmonic terms not present in our model become more significant, increasing κ and causing divergence from the usual T^{-1} dependence [19].

GeTe has a large electronic contribution to the total thermal conductivity. Nath *et al.* [20] and Levin *et al.* [15] estimated the lattice contribution by subtracting the electrical contribution from the measured total thermal conductivity using the Wiedemann-Franz law. Within a temperature range of 100-300 K, our computed κ is in very good agreement with that of a 9000 Å GeTe film with a hole concentration of $\sim 10^{20}$cm^{-3} measured using a

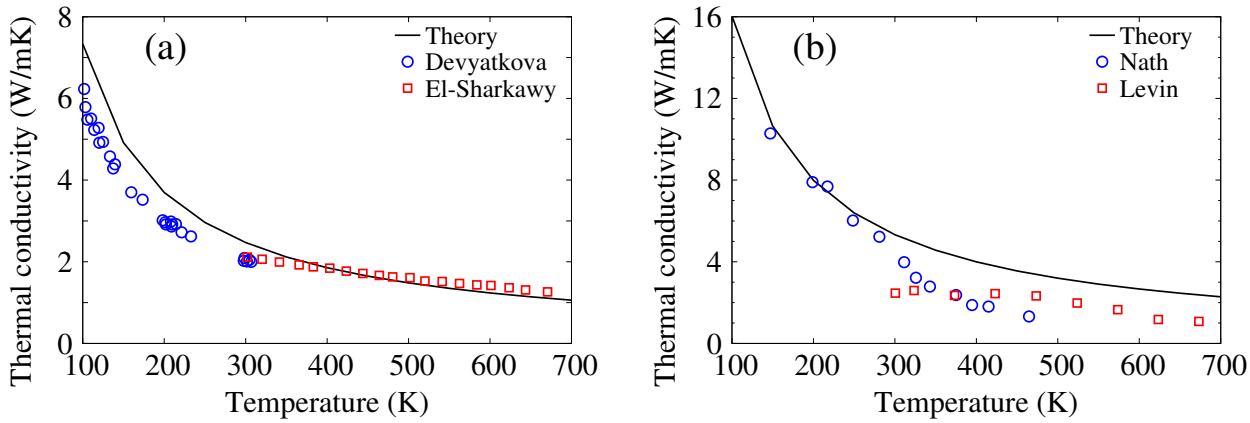

FIG. 4. (a) Lattice thermal conductivity of PbTe as a function of temperature: calculated using a 128 atom supercell (solid black line), measured by Devyatkova *et al.* [17] (blue circles), and measured by El-Sharkawy *et al.* [18] (red squares), (b) Lattice thermal conductivity of GeTe as a function of temperature: calculated using a 128 atom supercell (solid black line), measured by Nath *et al.* [20] (blue circles), and measured by Levin *et al.* [15] (red squares).

transient technique [20], see Fig. 4 (b). However, for 300-500 K the κ of the same GeTe film measured using a steady-state technique [20] is by up to a factor of ~ 2 lower than our calculated κ. Our results are also up to ~ 2 times higher than the κ of GeTe with a hole concentration of $\sim 8\times 10^{20}\text{cm}^{-3}$ measured with the flash thermal diffusivity method [15] for 300-700 K. However, our model does not capture the phase transition in GeTe from the rhombohedral to rocksalt phases at ~670 K [15, 21] due to the zero temperature representation of structural parameters and IFCs. Thus, we would expect some disagreement between our calculations and the experimental data at higher temperatures.

III. STRUCTURAL PROPERTIES

The total energy of both rocksalt and rhombohedral phases versus Ge concentration, as well as their energy difference, are illustrated in Fig. 5. The two curves coincide for $x < 0.492$ since the rocksalt phase is a special case of the rhombohedral phase with the relative Te position of $(0.5, 0.5, 0.5)$ within the primitive unit cell, and the angle between the primitive lattice vectors of 60°. In the rhombohedral lattice, the relative position of the second atom is $(0.5 + r, 0.5 + r, 0.5 + r)$, and the angle is $60° - \theta$. The rocksalt phase thus corresponds

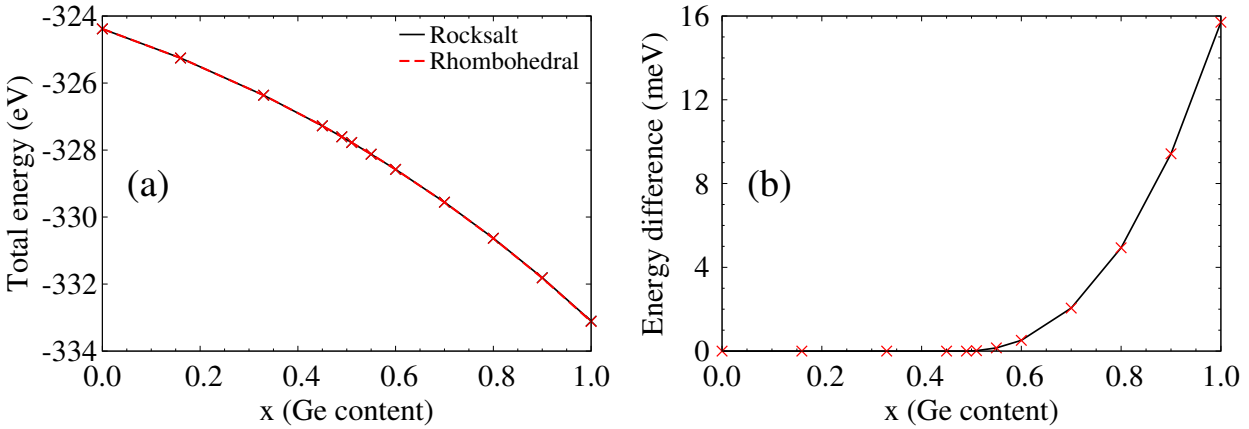

FIG. 5. (a) Total energy of the rocksalt and rhombohedral phases of $Pb_xGe_{1-x}Te$ as a function of the alloy composition x. (b) Difference between the total energy of the rocksalt and rhombohedral phases as a function of x. The rocksalt structure is a special case of the rhombohedral structure, and they are identical for $x < 0.492$.

to the rhombohedral phase with $r = 0$ and $\theta = 0°$. Consequently, the relaxation of the rhombohedral structure for $x < 0.492$ results in the rocksalt structure, which is consistent with the second order phase transition. For $x > 0.492$, the rhombohedral phase has a lower energy than the rocksalt phase.

Fig. 6 shows the calculated structural parameters as a function of the $Pb_{1-x}Ge_xTe$ alloy composition. The lattice constant, the angle between the primitive lattice vectors, and the Te position along the [111] direction all vary continuously as a function of the alloy composition, as expected for the second-order phase transition. Te displacement changes most rapidly with the alloy composition, indicating that it is the primary order parameter for this phase transition.

IV. TRANSVERSE OPTICAL MODES NEAR THE PHASE TRANSITION

We found a factor of $\sim \sqrt{2}$ difference between the transverse optical (TO) frequencies at Γ for the rhombohedral and rocksalt $Pb_{1-x}Ge_xTe$ alloys very near the phase transition: $x = 0.493$ and $x = 0.491$, respectively. To explain this factor analytically, we examine the total energy of the atomic motion of the TO mode in $Pb_{1-x}Ge_xTe$ virtual alloys, which can be represented by the displacement of Te atom from its equilibrium position in the rocksalt

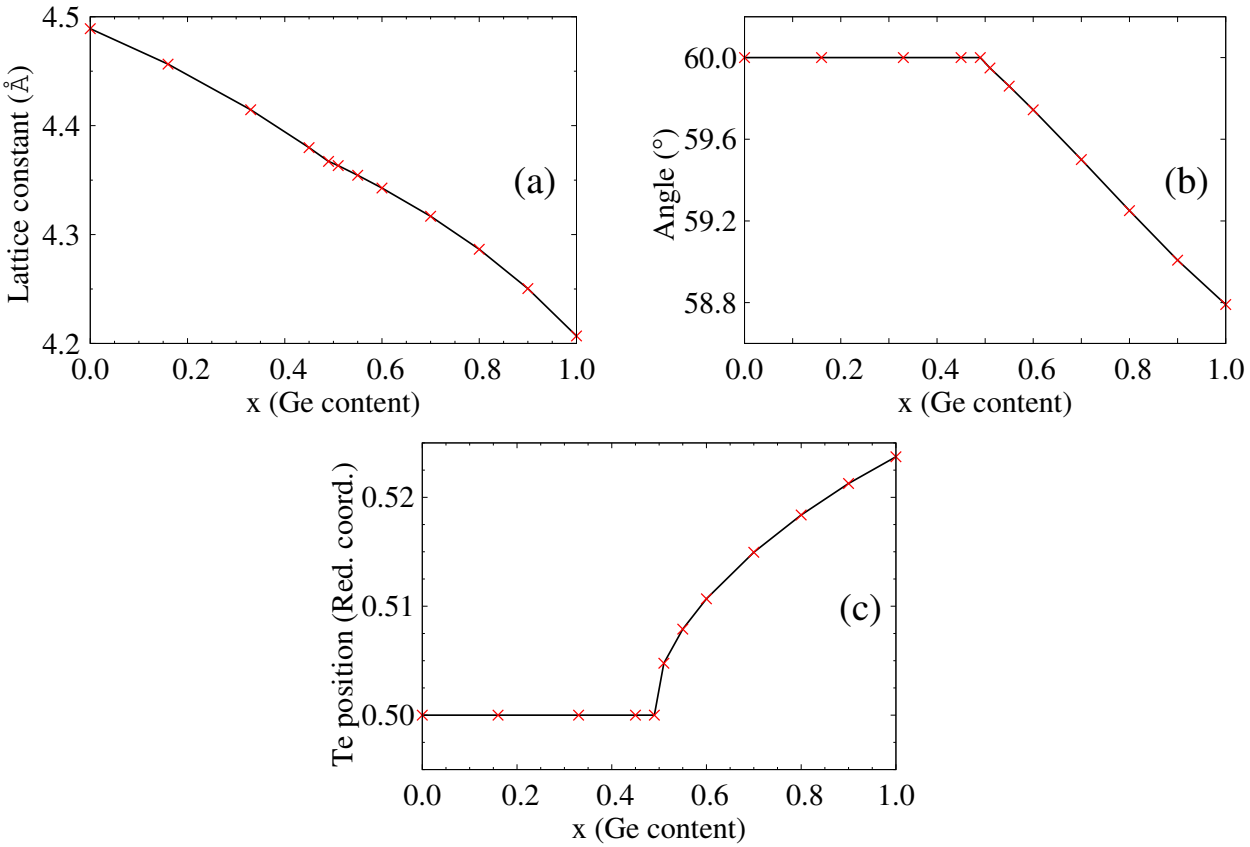

FIG. 6. Calculated structural parameters as a function of $Pb_{1-x}Ge_xTe$ alloy composition: (a) lattice constant, (b) rhombohedral angle, and (c) Te position along the [111] direction in the crystal lattice coordinates.

structure along the [111] direction. We assume that the energy potential of such Te motion is of the form:

$$V(z) = \frac{1}{2}kz^2 + Az^4,$$

where k and A are the harmonic and quartic spring constants, respectively. Near the phase transition, we assume that the small harmonic spring constant k changes its sign from positive to negative, keeping the same absolute value. This physically corresponds to changing the sign of a small restoring force which keeps atoms in one phase when positive, and causes the transition into a different phase when negative. We assume that the anharmonic spring constant A is positive and does not change in this process.

We find the potential extrema from:

$$\frac{\partial V}{\partial z} = kz + 4Az^3 = 0,$$

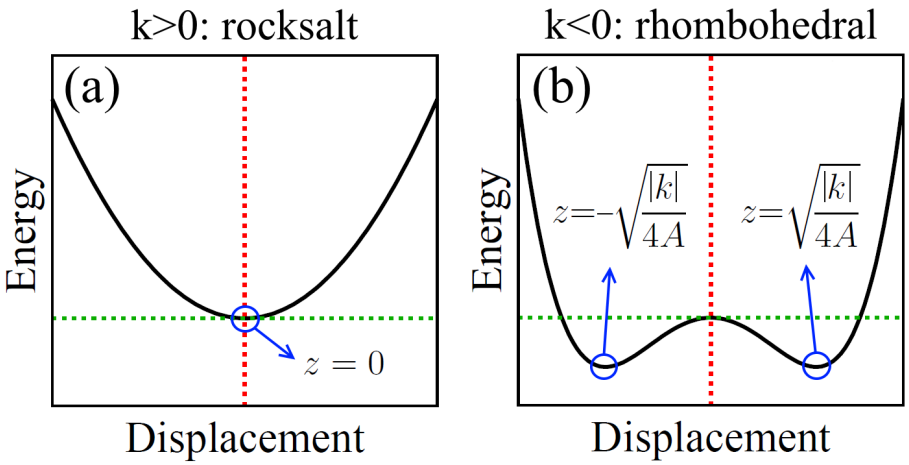

FIG. 7. Cartoon of the total energy versus Te atomic displacement from its equilibrium position in the rocksalt structure along the [111] direction for: (a) the rocksalt phase, and (b) the rhombohedral phase.

which gives

$$z = 0 \quad \text{or} \quad z = \pm i\sqrt{\frac{k}{4A}}.$$

For $k > 0$, $z = 0$ is the only real minimum, which physically corresponds to the high-symmetry rocksalt phase (see Fig. 7 (a)). For $k < 0$, $z = 0$ is a local maximum, and the minima occur for $z = \pm(|k|/(4A))^{1/2}$, which correspond to the frozen-in displacement of Te atom in the [111] direction and the distorted rhombohedral structure, shown in Fig. 7 (b).

Since the curvature of the potential varies as the square of the frequency ($\partial^2 V/\partial z^2 \sim \omega^2$), we find its values at the potential minima for the rocksalt phase at $z = 0$ and for the rhombohedral phase at $z = \pm(|k|/(4A))^{1/2}$:

$$\frac{\partial^2 V}{\partial z^2}\Big|_{z=0} = k = |k|, \quad k > 0;$$

$$\frac{\partial^2 V}{\partial z^2}\Big|_{z=\pm\sqrt{\frac{|k|}{4A}}} = 2|k|, \quad k < 0.$$

With $\partial^2 V/\partial z^2 \sim \omega_{\rm TO}^2$, we finally obtain:

$$\frac{\omega_{\rm TO}(x = 0.493)}{\omega_{\rm TO}(x = 0.491)} \sim \sqrt{2}.$$

Thus, the frequency of the TO mode at Γ differs by a factor $\sim \sqrt{2}$ between the rhombohedral

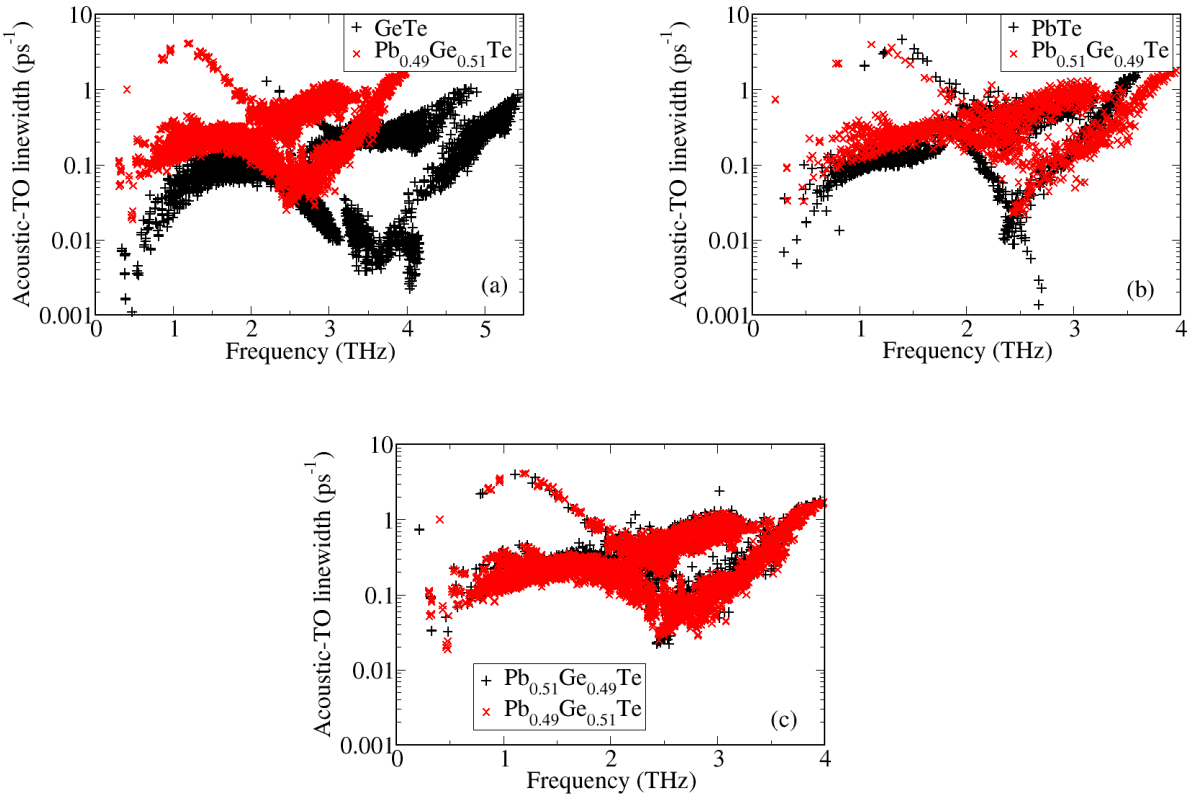

FIG. 8. The acoustic-transverse optical (TO) contribution to the total anharmonic linewidth at 300 K versus frequency for: (a) GeTe (black pluses) and a rhombohedral alloy near the phase transition, $Pb_{0.49}Ge_{0.51}Te$ (red crosses), (b) PbTe (black pluses) and a rocksalt alloy near the phase transition, $Pb_{0.51}Ge_{0.49}Te$ (red crosses), and (c) rocksalt $Pb_{0.51}Ge_{0.49}Te$ (black pluses) and rhombohedral $Pb_{0.49}Ge_{0.51}Te$ (red crosses).

$Pb_{1-x}Ge_xTe$ alloy very near the phase transition, $x = 0.493$, and its rocksalt counterpart, $x = 0.491$.

V. ACOUSTIC-OPTICAL COUPLING AT THE PHASE TRANSITION

To understand how the acoustic-TO anharmonic interaction changes with the increased proximity to the phase transition, we calculated explicitly the acoustic-TO contribution to the total anharmonic linewidth (inverse of the lifetime) in PbTe, $Pb_{0.51}Ge_{0.49}Te$, $Pb_{0.49}Ge_{0.51}Te$ and GeTe at 300 K. This contribution was computed for all phonon frequencies by accounting for the triplets of interacting states that contain at least one acoustic and

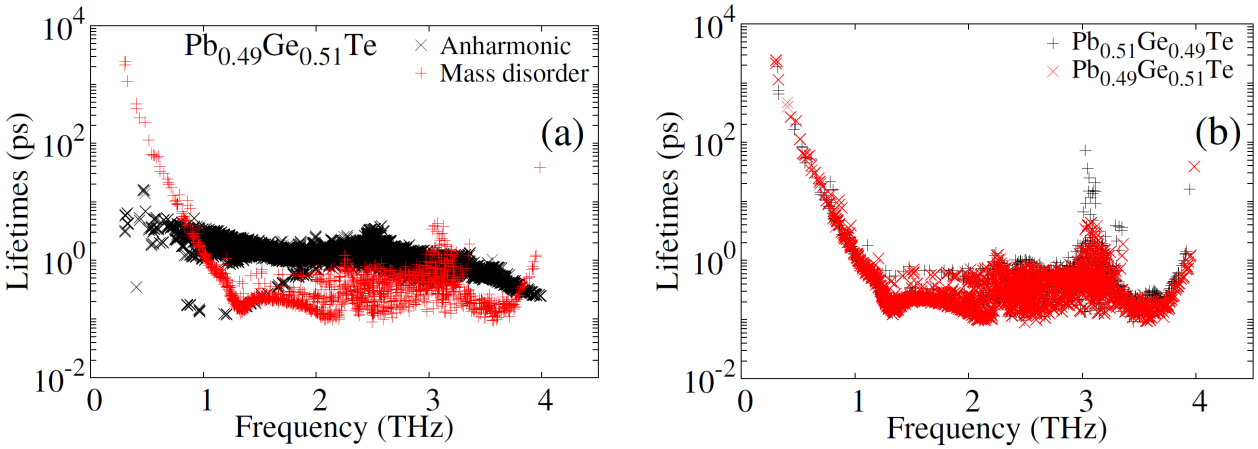

FIG. 9. (a) Phonon lifetimes due to anharmonic three-phonon interaction (black crosses) and mass disorder (red pluses) as a function of frequency for $Pb_{0.49}Ge_{0.51}Te$. (b) Phonon lifetimes due to mass disorder versus frequency for the rocksalt and rhombohedral structures very near the phase transition: $Pb_{0.51}Ge_{0.49}Te$ (black pluses) and $Pb_{0.49}Ge_{0.51}Te$ (red crosses), respectively.

one TO mode. For each wave vector, we labeled the two lowest phonon modes as transverse acoustic (TA) modes, and the highest mode as longitudinal optical (LO) mode. Since the ordering of TO and longitudinal acoustic (LA) modes changes throughout the Brillouin zone, we distinguished between them using the following procedure. We determined which one of those three states is mostly longitudinal by projecting their eigenvectors onto the corresponding wave vector, and classified it as LA mode, while the other two states were labeled as TO modes. We found that the acoustic-TO contribution to the anharmonic linewidth dominates over the other contributions across the spectrum in all these materials [22]. In the rhombohedral phase, this contribution becomes maximal at the phase transition, as illustrated in Fig. 8 (a) by comparing GeTe and an alloy composition very near the phase transition, $Pb_{0.49}Ge_{0.51}Te$. This finding also holds for the rocksalt phase, as shown in Fig. 8 (b) that compares PbTe and $Pb_{0.51}Ge_{0.49}Te$. The strength of the acoustic-TO contribution to the anharmonic linewidth is very similar for the two structures very close to the phase transition, see Fig. 8 (c), which is a typical feature of the second-order phase transition.

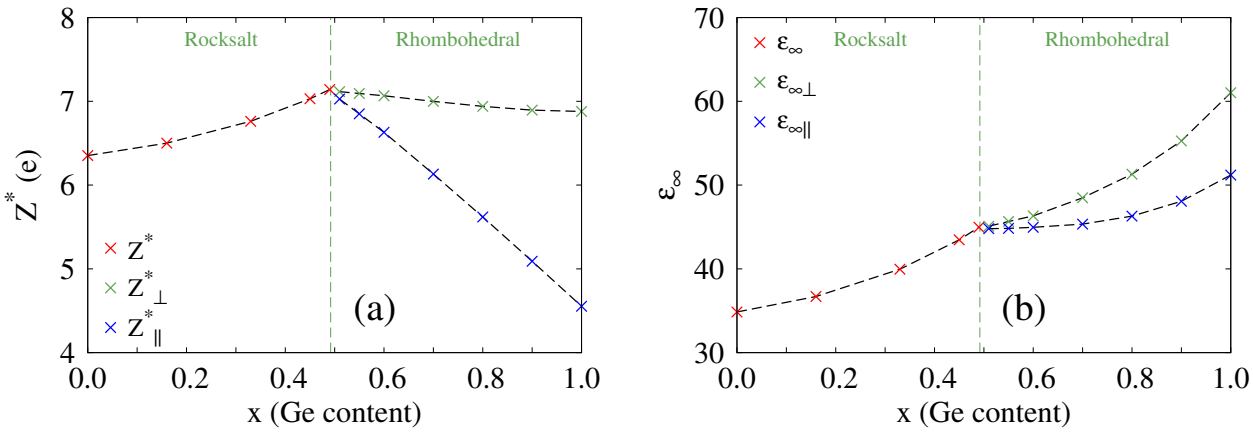

FIG. 10. (a) Born effective charge as a function of $Pb_{1-x}Ge_xTe$ alloy composition in the rocksalt phase (red crosses), perpendicular to the trigonal [111] axis in the rhombohedral phase (green crosses), and parallel to the trigonal axis in the rhombohedral phase (blue crosses). (b) High-frequency dielectric constant as a function of $Pb_{1-x}Ge_xTe$ alloy composition in the rocksalt phase (red crosses), perpendicular to the trigonal axis in the rhombohedral phase (green crosses), and parallel to the trigonal axis in the rhombohedral phase (blue crosses).

VI. ANHARMONIC PROCESSES AND MASS DISORDER

Anharmonic three-phonon interaction is more effective at scattering low frequency phonons, and mass disorder is more efficient at scattering higher frequencies. These effects are illustrated in Fig. 9 (a) for the rhombohedral $Pb_{0.49}Ge_{0.51}Te$ very near the phase transition. Furthermore, the lifetimes due to mass disorder of the rocksalt and rhombohedral structures on the verge of the phase transition are very similar as a result of the second-order nature of the phase transition, see Fig. 9 (b).

VII. ELECTRONIC POLARIZABILITY

The electronic polarizability of $Pb_{1-x}Ge_xTe$ alloys is maximized at the phase transition, which is indicative of very strong resonant bonding [23–25]. This is illustrated by plotting Born effective changes (BECs) as a function of the alloy composition, Fig. 10 (a). BECs are typically viewed as an indicator of ferroelectric instability, and have been found to be considerably larger than nominal ionic values in ferroelectric or nearly ferroelectric materials [26–28]. In the case of $Pb_{1-x}Ge_xTe$ alloys, BECs are more than twice the nominal ionic value

of +2 for Pb and Ge, and -2 for Te. As proximity to the phase transition is increased, there is a considerable increase in BECs, indicative of the increase in electronic polarizability. The high-frequency dielectric constants are also large in $Pb_{1-x}Ge_xTe$ alloys (Fig. 10 (b)), further illustrating the large electronic polarizability. The dielectric constants increase substantially, almost doubling in value from PbTe to GeTe, due to their inverse dependence on the average electronic gap [29].

[1] W. Cochran, R. A. Crowley, G. Dolling, and M. M. Elcombe, Proc. R. Soc. Lond. A **293**, 433 (1966).

[2] P. Fons, A. V. Kolobov, M. Krbal, J. Tominaga, K. S. Andrikopoulos, S. N. Yannopoulos, G. A. Voyiatzis, and T. Uruga, Phys. Rev. B **82**, 155209 (2010).

[3] E. Steigmeier and G. Harbeke, Solid State Commun. **8**, 1275 (1970).

[4] U. D. Wdowik, K. Parlinski, S. Rols, and T. Chatterji, Phys. Rev. B **89**, 224306 (2014).

[5] P. Bauer Pereira, I. Sergueev, S. Gorsse, J. Dadda, E. Müller, and R. P. Hermann, Phys. Status Solidi B **250**, 1300 (2013).

[6] R. Shaltaf, E. Durgun, J.-Y. Raty, P. Ghosez, and X. Gonze, Phys. Rev. B **78**, 205203 (2008).

[7] D. A. Broido, A. Ward, and N. Mingo, Phys. Rev. B **72**, 014308 (2005).

[8] G. P. Srivastava, *The Physics of Phonons* (Taylor & Francis Group, New York, U.S.A., 1990).

[9] R. Dalven, Infrared Phys. **9**, 141 (1969).

[10] B. Houston, R. E. Strakna, and H. S. Belson, J. Appl. Phys. **39**, 3913 (1968).

[11] P. K. Schelling and P. Keblinski, Phys. Rev. B **68**, 035425 (2003).

[12] T. Chattopadhyay, J. X. Boucherle, and H. G. von Schnering, J. Phys. C **20**, 1431 (1987).

[13] T. Chatterji, C. M. N. Kumar, and U. D. Wdowik, Phys. Rev. B **91**, 054110 (2015).

[14] D. Yang, T. Chatterji, J. A. Schiemer, and M. A. Carpenter, Phys. Rev. B **93**, 144109 (2016).

[15] E. M. Levin, M. F. Besser, and R. Hanus, J. Appl. Phys. **114**, 083713 (2013).

[16] H. Wiedemeier and P. A. Siemers, Z. Anorg. Allg. Chem. **431**, 299 (1977).

[17] E. D. Devyatkova and I. A. Smirnov, Sov. Phys. Solid State, USSR **3**, 1666 (1962).

[18] A. A. El-Sharkawy, A. M. A. El-Azm, M. I. Kenawy, A. S. Hillal, and H. M. Abu-Basha, Int. J. Thermophys. **4**, 261 (1983).

[19] A. H. Romero, E. K. U. Gross, M. J. Verstraete, and O. Hellman, Phys. Rev. B **91**, 214310 (2015).

[20] P. Nath and K. L. Chopra, Phys. Rev. B **10**, 3412 (1974).

[21] D. K. Hohnke, H. Holloway, and S. Kaiser, J. Phys. Chem. Solids **33**, 2053 (1972).

[22] R. M. Murphy, E. D. Murray, S. Fahy, and I. Savić, Phys. Rev. B **93**, 104304 (2016).

[23] S. Lee, K. Esfarjani, T. Luo, J. Zhou, Z. Tian, and G. Chen, Nat. Comm. **5**, 3525 (2014).

[24] G. Lucovsky and R. M. White, Phys. Rev. B **8**, 660 (1973).

[25] P. B. Littlewood and V. Heine, J. Phys. C **12**, 4431 (1979).

[26] W. Zhong, R. D. King-Smith, and D. Vanderbilt, Phys. Rev. Lett. **72**, 3618 (1994).

[27] P. Ghosez, J. P. Michenaud, and X. Gonze, Phys. Rev. B **58**, 6224 (1998).

[28] U. V. Waghmare, N. A. Spaldin, H. C. Kandpal, and R. Seshadri, Phys. Rev. B **67**, 125111 (2003).

[29] M. S. Hybertsen and S. G. Louie, Phys. Rev. B **35**, 5585 (1987).